

Self-consistent Coulomb picture of an electron-electron bilayer system

A. Siddiki

Physics Department, Arnold Sommerfeld Center for Theoretical Physics, and CeNS, Ludwig-Maximilians-Universität München, Theresienstrasse 37, D-80333 München, Germany

(Received 31 August 2006; revised manuscript received 11 January 2007; published 10 April 2007)

In this work we implement the self-consistent Thomas-Fermi approach and a local conductivity model to an electron-electron bilayer system. The presence of an incompressible strip, originating from screening calculations at the top (or bottom) layer is considered as a source of an external potential fluctuation to the bottom (or top) layer. This essentially yields modifications both on the screening properties and on the magnetotransport quantities. The effects of the temperature, interlayer distance, and density mismatch on the density and the potential fluctuations are investigated. It is observed that the existence of the incompressible strips plays an important role simply due to their poor screening properties both on the screening and the magnetoresistance properties. Here we also report on and interpret the observed magnetoresistance hysteresis within our model.

DOI: [10.1103/PhysRevB.75.155311](https://doi.org/10.1103/PhysRevB.75.155311)

PACS number(s): 73.20.-r, 73.50.Jt, 71.70.Di

I. INTRODUCTION

The successful experimental realization of a two-dimensional electron system (2DES) has revealed a technique to exploit the quantum mechanical properties of a wide range of mesoscopic systems, including the integer quantized Hall effect¹ (IQHE) and the *drag*² effect. An interesting composite two-dimensional (2D) charge system to study screening and magnetotransport is the so-called bilayer system. The basic idea is to bring two 2DESs into a close proximity, in parallel to each other, perpendicular to the growth direction. For such a system, it was predicted that transport in the active layer will drive the passive layer out of equilibrium. Even if the barrier separating the two layers is high and wide enough to prevent tunneling, the interlayer interactions can still be sufficiently strong. This effect is known as the *drag effect*.² With the improvement of the experimental techniques, an additional electron or hole layer was also accessible to measure the magnetotransport quantities of the bilayer systems. Motivated by the *drag effect* experiments,³⁻⁸ both the electrostatic and the transport properties of such bilayer systems were investigated theoretically⁹⁻¹⁵ within the independent electron picture, however, the self-consistent treatment of screening was left unresolved. Recently, a magnetoresistance (MR) hysteresis has been reported for the 2D bilayer systems¹⁶⁻²⁰ under quantum Hall (QH) conditions. For the GaAs hole bilayer system, Tutuc *et al.*^{17,18} observed hysteretic longitudinal resistance at the magnetic field positions, where either the majority (higher density) or the minority (lower density) layer is at Landau level (LL) filling one. They have argued that the hysteresis is due to a layer-charge instability, which creates domains at different layer densities, although the origin and the details of the domains were not discussed. For the electron bilayer system Pan *et al.* concluded that the observed hysteresis is due to a spontaneous charge transfer via the ohmic contacts. So far no explicit calculations were provided to account for the experimental findings in the context of the standard pictures of the IQHE, which is usually explained within the single particle picture. These models rely on the fact that the system is disordered and localization is essential.²¹ For a homogeneous 2DES,

incorporating the disorder results in broadening of the LLs (due to scattering) and yields to a finite longitudinal conductance (σ_l). Meanwhile, the long range potential fluctuations generated by the disorder result in the so-called *classical localization*. On the other hand, within the Landauer-Büttiker approach (known as the 1D edge channel picture²²) one also needs localization assumptions in order to obtain QH plateaus of finite width (see for a review, e.g., Datta's book²³). To our knowledge, this model is not applied to a bilayer system where a hysteresis is observed and, indeed, it may be questionable to implement it to such a nonequilibrium case.

The experimental work of Ahlswede *et al.*^{24,25} provided important and unexpected information about the Hall voltage (and thereby current) distribution in relatively narrow ($\approx 15 \mu\text{m}$) single layer Hall bars. In these experiments a scanning force microscope was used to probe locally the Hall potential across a narrow Hall sample. The measurements were performed in different regimes of the magnetic field, B , around the QH plateaus corresponding to small integer values of the LL filling factors, $\nu = \phi_0 \bar{n}_{e1} / B$, where $\phi_0 = 2\pi\hbar c / e$ is the magnetic flux and \bar{n}_{e1} the average electron density. They found that far from integer filling, the Hall potential drops linearly across the sample (type I), whereas in the immediate neighborhood of an integer filling, one observes a strong nonlinear drop in the center of the sample (type II). At lower B values, within the QH plateau, the Hall potential is constant at the bulk and the drops occur close to the edges (type III). These potential variations exactly coincide with the predicted^{26,27} positions of the ISs, however, *only a single IS* was observed at an edge, which is in agreement with Hartree type self-consistent calculations considering the finite extent of the wave functions.²⁸⁻³⁰ On the other hand, the findings of the experiments are not in agreement with the above-mentioned bulk (localization) and edge channel approaches, since they clearly demonstrate that the current can flow both from the bulk (type I,II) and the edge, from a single channel (type III), depending on the magnetic field strength. The clear identification of the local potential drops also point to the necessity of a *local conductivity* model. Motivated by these experiments Gerhardtts and his co-workers have developed a microscopic model, which al-

lowed them to treat narrow Hall samples without^{27,31,32} and with^{29,33–35} dissipative currents. They were able to calculate self-consistently the electron density, potential, and current density distributions in the relevant 2DESs, taking into account the electron-electron ($e-e$) interactions within Hartree type approximations. They have calculated in a first step the electron density $n_{el}(x)$ and effective electrostatic potential $V(x)$ for a narrow, in y direction, translational invariant 2DES within a self-consistent Thomas-Fermi-Poisson approach (SCTFPA) for an equilibrium situation with constant electrochemical potential μ^* . As a result of self-consistent screening calculations the 2DES splits into two domains, namely the quasimetallic compressible and quasi-insulating incompressible regions. The electron distribution within the Hall bar depends on the pinning of the Fermi level to the highly degenerate Landau levels. As expected, if the Fermi level is equal to (within a few $k_B T$, k_B is the Boltzmann constant and T the temperature) a LL with high density of states (DOS) the electron system is known to be compressible (locally), otherwise incompressible. In the next step, they have imposed an external current, assuming a local version of the Ohm's law, $\vec{j}(x) = \hat{\sigma}(x)\vec{E}(x)$, for the relation between the current density $\vec{j}(x)$ and the driving electric field $\vec{E}(x)$. For the position dependent conductivity tensor $\hat{\sigma}(x)$ a result for a homogeneous system of electron density n_{el} is taken and is replaced by $n_{el}(x)$. The essence of this model relies on the fact that it is free from any localization assumptions and is fairly independent of the details of the DOS and thereby the conductivity model considered. This local model also successfully facilitated the investigation of the spatial distribution of the electron temperature, including the breakdown regime.³⁶ We will briefly represent this local model, while discussing the MR curves (in Sec. IV) calculated for an $e-e$ bilayer system. The verification of the above assumptions, about the local Ohm's law and confinement of the current into the incompressible strips (ISs), is clarified by the above-mentioned experiments and also by recent experimental results of Yacoby *et al.*, where a single electron transistor is used to probe locally the transparency,³⁷ the compressibility, and resistivity³⁸ of the 2DES under QH conditions. In particular, it is shown that the local longitudinal resistivity vanishes within the ISs (see especially Fig. 1d of Ref. 38), therefore the current is confined to these regions in certain B intervals, namely within the QH plateau regimes. We should also mention that the microscopic model described above is valid if the external potential (including disorder potential) is slowly varying in the length scales compared to the magnetic length or Fermi wavelength and for relatively narrow ($\leq 10 \mu\text{m}$ for low mobility and $\leq 100 \mu\text{m}$ for high mobility) Hall samples. In the case of large and highly disordered samples (and low magnetic fields) the main scattering processes are due to the disorder potential, hence the IS picture may not be applicable and the standard model of the IQHE is restored. Throughout this work we will consider samples which do clearly satisfy the above conditions, i.e., narrow and high mobility samples.

In a very recent experiment a magnetotransport hysteresis was observed³⁹ at an $e-e$ bilayer system, similar to the one measured at a single layer⁴⁰ and at a bilayer.²⁰ The single

layer case was attributed to the thermodynamical nonequilibrium caused by the ISs and it was concluded that the 2DES cannot be considered in the thermodynamic equilibrium at the plateau regimes when measuring the Hall resistance while sweeping the magnetic field. A similar argument is also given in Ref. 16 for a 2DES coupled to a 2D impurity channel. In the theoretical investigation of the bilayer system,³⁹ specific attention was paid to the nonequilibrium situation. It was simulated by frozen potential profiles and a qualitative explanation was provided.³⁹ However, the screening properties of the 2DES was not discussed in detail, which indeed is essential to achieve a quantitative understanding of the underlying physics of the inter- and intra-layer $e-e$ interactions. In this paper we apply and extend the self-consistent scheme developed by Gerhardtts and his co-workers^{29,33–35,41} to a bilayer system and provide explicit Coulomb interaction calculations. For this model system, we investigate both the screening and the magnetotransport properties within the linear response regime under QH conditions. We show that the existence of the incompressible regions in one of the layers effects the other layer density profile strongly by creating potential fluctuations. We observe that these potential fluctuations modify the magnetotransport quantities. Here we present our model in more detail that explains some of the recent experimental findings,³⁹ where the magnetotransport hysteresis was observed for mismatched densities, whenever one of the layers is in the QH plateau regime.

The organization of this work is as follows: first the bilayer geometry, a model Hamiltonian describing the system and the SCTFPA are introduced in Sec. II. Second, we discuss the electron density and electrostatic potential profiles obtained within the screening model. In particular, we systematically investigate the influence of the ISs depending on temperature, interlayer distance, and the density mismatch on the electrostatic properties (Sec. III) of the bilayer system. In Sec. IV, we represent and use the scheme proposed by Siddiki and Gerhardtts (SG)²⁹ to calculate the Hall and the longitudinal resistances. We examine the effects of the ISs from the point of external potential fluctuations based on the fact that a perturbing external potential may shift, widen, and/or stabilize the QH plateaus. We explicitly observe such a widening due to the potential fluctuations generated by the ISs and relate it to the measured MR hysteresis in Sec. V. A summary and a discussion on further open questions concludes our work.

II. THE GEOMETRY AND MODEL HAMILTONIAN

In a typical electron bilayer sample, a silicon doped thick (AlGa)As layer is grown on top of a GaAs substrate. This is followed by the bottom GaAs quantum well, separated from the top 2DES by an undoped AlGaAs spacer. On top of the upper 2DES again a silicon doped (AlGa)As layer is grown, which is capped by a GaAs layer; so that two 2DES are placed in close proximity, which are confined by remote donors and the sample is capped by top and/or bottom gates that control the electron density of each layer. In the related experiments both gates are used to tune the electron densities of the top and the bottom layers. Note that the gate potential

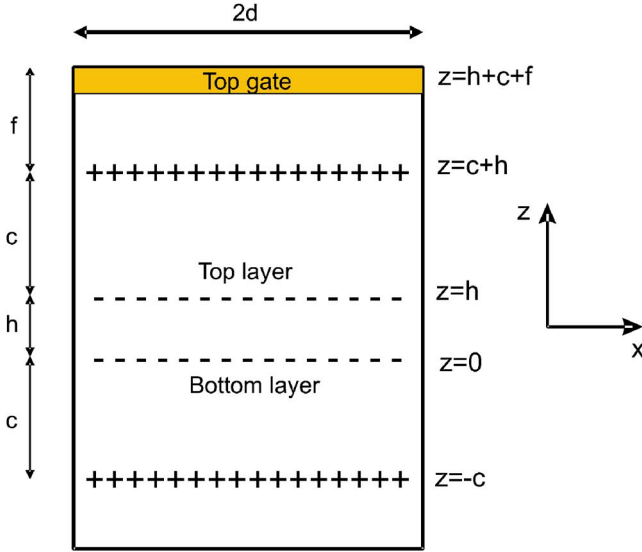


FIG. 1. (Color online) The cross section of the bilayer geometry. The sample is capped by a gate from the top in order to manipulate the electron density of the top layer. Top (bottom) 2DES lies below (above) the top (bottom) layer donors at a distance c . Electron layers are separated from each other by a dielectric spacer having thickness h .

profile depends on the sample geometry and the applied gate bias. The electrons are symmetrically (with respect to the growth direction) confined by AlGaAs layers each of which contains a plane of Si doping (δ -doping), and are separated by a spacer of thickness h (~ 10 – 30 nm). For such a separation thickness, the bilayer system is then known to be electronically decoupled and in electrochemical nonequilibrium, i.e., it can be represented by two different electrochemical potentials. Electron tunneling between the layers is not possible^{17,20,39,42} since the resistance between the layers can be as large as 100 M Ω . The same structure was investigated in Ref. 39 in the context of thermodynamic nonequilibrium and it was ascertained experimentally that the two electron layers are not connected to establish a charge equilibrium via tunneling or contacts.

In Fig. 1 a schematic drawing of a mesa etched bilayer system is shown, which consists of two 2DESs (minus signs), two donor layers (plus signs), and a top gate (shaded, yellow area). We model the bilayer system such that the bottom 2DES lies on the $z=0$ plane with a number density $n_{\text{el}}^{\text{B}}(x)$ in the stripe $-d < x < d$, where $2d$ is the width of the sample and the top layer is in the plane $z=h$, with the electron density $n_{\text{el}}^{\text{T}}(x)$. Relevant to the considered experiments, we assume that the donors are symmetrically separated from the electron layers placed at $z=-c$ and $z=c+h$, for the bottom and the top layers, respectively, having a constant surface density $n_0^{\text{T}}=n_0^{\text{B}}=n_0$. Here we also assume translation invariance in the y direction. The electron density of the top 2DES is governed by the top gate, located at $z=c+h+f=z_g$ and the electron channels are formed in the interval $|x| \leq b$.

Next, we introduce a generic Hamiltonian which describes the above model for the general case, which includes many of the possible contributions to the total energy of the system. We then drop some of the terms by considering spin-

less electrons and discuss the effects of the dominant terms. In general, the Hamiltonian is composed of the kinetic H_0 , the external $V_{\text{ext}}(\mathbf{r})$, the interaction $V_{\text{int}}(\mathbf{r})$ potentials, and Zeeman energy terms,³⁰

$$H^\sigma = H_0 + V_{\text{int}}^\sigma + V_{\text{ext}} + V_Z^\sigma, \quad (1)$$

where $\mathbf{r}=(x,y,z)$ is the three-dimensional position and $\sigma(=\pm 1/2)$ is the spin degree of freedom. For the GaAs/AlGaAs heterostructures the effective band g factor ($=-0.4$) is comparatively small, therefore Zeeman energy is much smaller than the cyclotron energy ($\hbar\omega_c$, with $\omega_c = eB/m^*c$, $-e, m^*$ electron charge and effective mass, respectively, and c the speed of the light in vacuum), i.e., $|g^* \mu_B B| / \hbar\omega_c \approx 0.027$, where μ_B is the Bohr magneton. Thus one can neglect the Zeeman splitting if the exchange and correlation effects (ECEs) can also be neglected. Throughout our calculations we will assume spinless electrons, hence we will be able to neglect the ECEs. Considering spinless electrons is justified with the experiments conducted by Tutuc *et al.*, in which they probed the effect of the spin degree of freedom by tilted magnetic field measurements. The results ruled out the possibility that the hysteresis observed originates from spin degree of freedom,¹⁷ therefore our assumption of spinless electrons and neglecting the ECEs become reasonable for the considered experiments. However, in principle the many-body effects are also important in exploring the IQHE.^{30,43–45} Unfortunately, the inclusion of the ECEs requires quite complicated calculations and the essential physics concerning the electron densities can already be governed by rather simple Hartree type approximations.⁴⁵ The qualitative agreement between the local model and the experimental findings also assures such a simplification.³⁹ The fact is that the ECEs may become fairly important to understand the effects of the electron spin on the subband structures. At first glance it is well-known that the exchange interaction enhances the spin splitting (even overestimates, without correlation) and may lead to a negative sign of the thermodynamic DOS. Moreover, the LLs can also be broadened due to exchange interaction, which will effect the screening properties of the 2DES.⁴⁴ Recently a local spin density approximation (LSDA) plus density functional theory (DFT) scheme was proposed by Zozoulenko and his co-workers and was implemented to couple 2DESs^{45–47} successfully. Such a treatment of many-body effects in a bilayer system is not possible at present, thus throughout this work we will consider only spinless electrons and neglect exchange and correlation effects, since we are mainly interested in the electron densities and the Coulomb interaction between them. We will calculate the electron density and the electrostatic potentials within the SCTFA yielding similar results of the Hartree-Fock type approximations.⁴⁵ Assuming the widely used simplification of the translational invariance in the y -direction, the effective Hamiltonian is reduced to

$$H^{\text{eff}} = H_0 + V_{\text{ext}}(x,z) + V_{\text{int}}^{\text{eff}}(x,z), \quad (2)$$

where H_0 is the single particle Hamiltonian of an electron subject to a magnetic field in the z -direction, $V_{\text{ext}}(x,z)$ is composed of the background and the disorder potentials cre-

ated by the donors, together with the (top) gate potential and the interaction term $V_{\text{int}}^{\text{eff}}(x, z)$ is the sum of the Coulomb interaction of the electrons within and between the layers, which we will introduce in detail in the next sections.

A. The kinetic energy

The single particle kinetic energy in the presence of a perpendicular magnetic field represented by the vector potential $\mathbf{A}(\mathbf{r})[(=\mathbf{0}, \mathbf{B}\mathbf{x}, \mathbf{0})$, in the Landau gauge] reads

$$H_0 = \frac{1}{2m^*} \left(\mathbf{p} + \frac{e}{c} \mathbf{A} \right)^2 \quad (3)$$

with the eigen (Landau) energies

$$E_n(X) = \hbar \omega_c (n + 1/2), \quad (4)$$

where X is the center coordinate defined as $X = -l^2 k_y$, $l = \sqrt{\hbar/m^* \omega_c}$ the magnetic length, k_y momentum in the y -direction, and n the Landau index. The eigenfunctions $\Phi_{n,X}(x, y)$ are obtained such that

$$\Phi_{n,X}(x, y) = L_y^{-1/2} \exp(iy k_y) \phi_{n,X}(x) \quad (5)$$

where $L_y^{-1/2}$ represents a normalization constant and $\phi_{n,X}(x)$ is the well-known Landau wave function. In the next section we will exploit the smoothness of the external potential (Sec. II B) and employ the Thomas-Fermi approximation (TFA) which essentially yields similar results of the density profiles of the Hartree approximation.^{28,29,41,45} The TFA is much simpler than the corresponding full quantum mechanical treatment of the 2DES, since the Landau wave functions are replaced by the Dirac delta functions, i.e., $|\phi_{n,X}(x)|^2 \approx \delta(x-X)$, and the center coordinate dependent eigenvalues are given in the lowest order perturbation as

$$E_n(X) \approx E_n + V(X). \quad (6)$$

Therefore the numerical effort is extremely reduced, meanwhile the electrostatic properties are well-represented.

B. Boundary conditions and external potentials

The electron bilayer samples considered in this paper are chemically etched and the donors are placed at a finite distance (in the z direction) from the electron layers, thus the well-known Chklovskii²⁶ geometry cannot be used to represent the electrostatics and thereby the Green's functions, i.e., the kernel. In this work we implement similar boundary conditions to that of Chklovskii (*in-plane*) geometry, which is named as the *perpendicular gate* model.⁴¹ Within this model the 2DES is confined laterally by two equipotential planes placed at the physical edges of the sample perpendicular to the electron system. It was argued that this model represents the free standing mesa-etched quantum Hall samples well both for the single layer⁴¹ and for the bilayer³⁹ systems. The solution of the Poisson equation can be obtained using the image charge technique.⁴⁸ The main advantage of this model is, one can obtain the z dependency of the potential distribution explicitly and also it is not necessary to assume that the donors and the electrons reside on the same plane, like in the

in-plane model. For the given boundary conditions $V(x = \pm d, y, z) = 0$, due to a line charge at (x_0, z_0) the Green's function (the kernel) on the line (x, z) is expressed as

$$K(x, x_0, z, z_0) = -\frac{1}{2} \ln \left(\frac{\cos^2 \frac{\pi}{4d} (x + x_0) + \gamma^2}{\sin^2 \frac{\pi}{4d} (x - x_0) + \gamma^2} \right), \quad (7)$$

where the z dependence is given by $\gamma = \sinh(\pi |z - z_0| / 4d)$, due to a misprint a factor $1/2$ was missing in our previous work,⁴¹ although the numerics included this factor properly. It is straightforward to calculate the electrostatic background potential at (x, z) generated by a (constant) distribution of donors, n_0 , on the line (x_0, z_0) via

$$V_{\text{bg}}^{\text{T,B}}(x, z) = -\frac{2e^2}{\bar{\kappa}} \int_{x_l}^{x_r} dx_0 K(x, x_0, z, z_0) n_0(x_0, z_0), \quad (8)$$

where T, B is the layer index representing top or bottom, respectively, and $\bar{\kappa}$ an average background dielectric constant (~ 12.4 for GaAs samples). The total background potential is the sum of the donor potentials of the top and the bottom layer expressed as

$$V_{\text{bg}}^{\text{tot}}(x, z) = -\left(\frac{2e^2}{\bar{\kappa}} \int_{x_l}^{x_r} dx_0 K(x, x_0, z, c+h) n_0(x_0, c+h) + \frac{2e^2}{\bar{\kappa}} \int_{x_l}^{x_r} dx_0 K(x, x_0, z, -c) n_0(x_0, -c) \right). \quad (9)$$

In Fig. 2, the numerically calculated background potential for typical parameters is depicted. In order to obtain a (electron) density mismatch between the layers we introduce a gate on top of the bilayer system. It is assumed that the gate can be described by an induced charge distribution $n_g(x)$, residing on the plane $z_g = h + c + f$. Then, similar to the background potential, the gate potential can be written as

$$V_g(x, z) = \frac{2e^2}{\bar{\kappa}} \int_{-d}^d dx_0 K(x, x_0, z, z_g) n_g(x_0, z_g). \quad (10)$$

In order to obtain a flat (gate) potential profile at the bulk we choose the induced charge distribution as

$$n_g(x, z_g) = n_g^0 [1 + \alpha(x/d)^2], \quad (11)$$

where n_g^0 determines the strength of the gate potential whereas α gives the slope of the induced charge distribution. In Fig. 3 the distribution of the (positive) induced charges and the resulting potential profile is shown for an arbitrary slope ($\alpha=0.7$). One can add more electrons to the top layer by setting $n_g^0/n_0 = V_0/E_0$ to a positive value, while keeping the depletion length $d-b$ fixed at zero temperature and for vanishing magnetic field. It is clear that other models⁴⁹ can be used to define the gate similarly in a better way, however, the main interest of the present work is to simply achieve a density mismatch between the electron layers and at the same time preserve the boundary conditions, therefore the details of the induced charge distribution do not effect the general results presented. For example, in Ref. 39 the gate

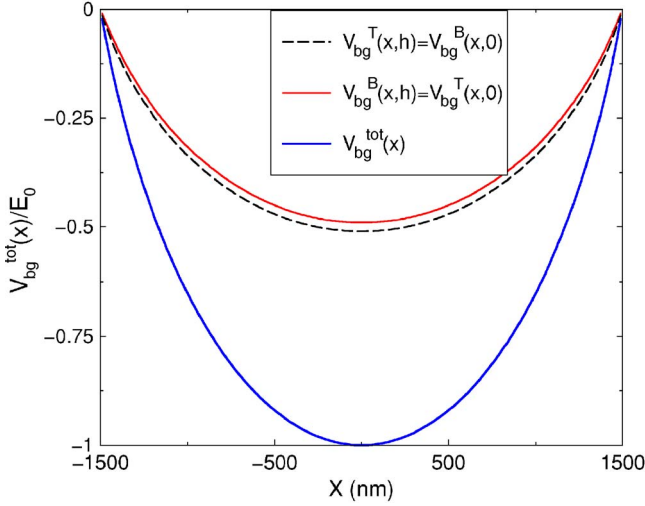


FIG. 2. (Color online) Total background potential created by the top and bottom layer donors (thick solid line). The potential contributions to the bottom 2DES ($z=0$) come from the top donor layer [$V_{bg}^T(x,0)$, thin solid line] and from the bottom donor layer [$V_{bg}^B(x,0)$, dashed line]. Numerical calculations are performed for the GaAs/(AlGa)As heterostructure with the parameters $h=15$ nm and $c=60$ nm. The numbers of donors are fixed to 4×10^{11} cm $^{-2}$ per layer, for a sample width $2d \sim 3$ μ m. The pinch-off energy is defined as $E_0 = (2\pi e^2 n_0 d / \bar{\kappa}) (\pi^2 / 8G)$ normalized with $G=0.915\ 965\ 594$, the Catalan's constant (Ref. 52) for $\gamma=0$.

was simulated by a cosine-hyperbolic type function and similar results were reported.

Similar to our previous works concerning single layer³⁵ and bilayer systems,³⁹ the strategy to include the disorder potential in our calculations is twofold: the long range (LR) part is added to the donor potential (the details are given in Sec. III C), whereas the short range (SR) part is included in

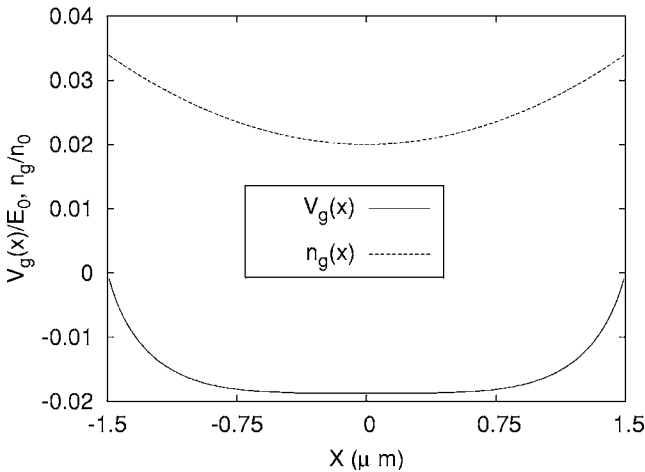


FIG. 3. The gate potential profile (solid line) at $z=h$, together with the generating positive charge distribution (dotted line) against position. The additional charges residing on the gate lead to a stronger confining potential in the top layer, resulting in a higher average electron density. The gate potential strength is taken to be $n_g^0/n_0 = V_0/E_0 = 0.02$. The donor density is $n_0 = 4 \times 10^{11}$ cm $^{-2}$. Other parameters are given in the text.

the conductivity model, implicitly. Before giving the justification of such a separation, we would like to make the definition of the short and long range clear. In the common theoretical description of the disorder potential the range is defined by the range of the single impurity potential, R , and is compared to the magnetic length l .⁵⁰ If $R < l$ the disorder is assumed to be SR, otherwise LR. On the other hand, experimentalists usually define the range of the disorder potential to be the range of the overall potential fluctuation, which can be large as micrometers for LR and is comparable with the Fermi wavelength for SR. This distinction becomes more pronounced when considering electronic screening and dielectric damping resulting from donor layer separation, i.e., the z dependence. Due to the nonlinear screening properties of the 2DES, the SR part remains (almost) unaffected after electronic screening (small Fourier components), however, it decreases exponentially with increasing z . Whereas the LR part is well-screened by the 2DES and is damped weakly with the increase of separation thickness. A detailed investigation of the LR (low-order Fourier components) and SR (high-order Fourier components) is given in Ref. 35 in context of the disorder and of the external potential in Ref. 51. Therefore we treat the SR part of the disorder potential as Gaussians and use the self-consistent Born approximation (SCBA) to obtain the DOS and conductivities, leaving it unaffected from screening. Meanwhile the LR part is included in the screening calculations via a modulation at the donor distribution.

In summary, the external potential is composed of the two donor layers, the top gate defined by the induced charges on the upper surface of the bilayer structure and the modulation (disorder) introduced by the donors. In the following we will name the sum of these potentials to be the total external potential and denote by $V_{ext}(x,z) = V_{bg}(x,z) + V_g(x,z) + V_m(x,z)$. It is clear that this potential is fixed by the parameters of the positive charges, e.g., n_0 , n_g , separation thickness, etc., and is insensitive to the changes of the magnetic field, whereas we will show that the interaction potential between the electrons is highly effected by the change of B , which will result in many interesting features observed at the screening and MR properties.

C. The e - e interaction and SCTFPA

The Coulomb interaction between the electrons can be calculated similar to the donors, gate, and disorder from Eq. (8) by replacing $-n_0$ with the electron density of each layer. This interaction (Hartree) term has two components, namely the intralayer

$$V_{intra}^{T,B}(x,z) = \frac{2e^2}{\bar{\kappa}} \int_{x_l}^{x_r} dx_0 K(x, x_0, z) n_{el}^{T,B}(x_0), \quad (12)$$

and the interlayer interaction

$$V_{inter}^{T,B}(x,z) = \frac{2e^2}{\bar{\kappa}} \int_{x_l}^{x_r} dx_0 K(x, x_0, z) n_{el}^{B,T}(x_0), \quad (13)$$

where the layer index defines the z_0 value, i.e., $z_0=0$ for the bottom and $z_0=h$ for the top layer. Then the total Hartree potential reads

$$V_H^{T,B}(x,z) = V_{\text{inter}}^{T,B}(x,z) + V_{\text{intra}}^{T,B}(x,z). \quad (14)$$

For example, the total electrostatic potential of an electron residing on the top layer is

$$V^T(x,h) = V_{\text{ext}}(x,h) + \frac{2e^2}{\bar{\kappa}} \int_{x_l}^{x_r} dx_0 K(x,x_0,h,h) n_{\text{el}}^T(x_0,h) + \frac{2e^2}{\bar{\kappa}} \int_{x_l}^{x_r} dx_0 K(x,x_0,h,0) n_{\text{el}}^B(x_0,0). \quad (15)$$

In the next step the electron densities are calculated within the TFA:

$$n_{\text{el}}^{T,B}(x) = \int dE D(E) f([E + V^{T,B}(x) - \mu_{T,B}^*]/k_B T), \quad (16)$$

with $D(E)$ the Landau density of states (DOS), $f(E) = 1/[\exp(E/k_B T) + 1]$ the Fermi function, and $\mu_{T,B}^*$ the chemical potential (being constant in the equilibrium state) of the top or the bottom layer, respectively. Throughout our screening calculations will use the bare Landau DOS, without loss of generality,^{33,41} described by

$$D(E) = \frac{1}{\pi l^2} \sum_{n=0}^{\infty} \delta(E - E_n), \quad (17)$$

as the default. In Sec. IV, where we calculate the resistances, we will reconsider the DOS and discuss in the context of SCBA. In our numerical calculations, we start with zero temperature and magnetic field and initially obtain the confining potential created by its own donors for each layer. Then, we obtain the electron densities and the total potentials of both layers just as in the case of a single layer.⁴¹ Knowing the electron distribution of the top (bottom) layer via Eqs. (15) and (16) we calculate the potential acting on the bottom (top) layer similar to the single layer case and vice versa. In each iteration step an accurate numerical convergency is achieved for a single layer, then the Hartree potential is added to the other layers external potential. Intralayer self-consistencies are obtained by Newton-Raphson iteration and interlayer self-consistency is obtained by direct iteration. One can then use this solution as an initial value and obtain the density and screened potential profiles for finite magnetic fields and temperatures.

The energies are scaled by the average pinch-off energy $E_0^* = (E_0^T + E_0^B)/2 = E_0$, since we always assume symmetric donor distribution, e.g., $\Omega_c = \hbar \omega_c / E_0$. The lengths are scaled by the screening length $a_0 (= a_B^*/2)$ expressed in terms of effective Bohr radius, $a_B^* = \bar{\kappa} \hbar^2 / (me^2)$. The electron densities and the electrostatic potentials can be calculated self-consistently by the above scheme within the TFA.

We conclude this section with the typical parameters used in the calculations. The lengths are $d=1570$ nm, $c=60$ nm, $h=15$ nm, $f=100$ nm, and $b=157$ nm, and will be kept fixed all through the paper (except h to investigate the effect of layer separation). The densities for the donors are $n_0=4 \times 10^{11}$ cm⁻² and for the unbiased gate, electron densities are set to be $\bar{n}_{\text{el}}^T = \bar{n}_{\text{el}}^B = 3.31 \times 10^{11}$ cm⁻² which result in a Fermi energy (E_F) ~ 14 meV. The depletion length is always kept

fixed and set to be 10% of the sample width, i.e., $|(d-b)/d|=0.1$. A positive (with respect to the electrons) potential bias is applied to the top gate [for details check Eq. (11) and related text] so that more electrons are populated to the top layer resulting in a density mismatch. The slope of the induced charge distribution, $\alpha(=0.7)$, is set to be a constant such that the resulting gate potential is flat at the bulk. We remind that this description of the gate is not unique therefore other gate models or α values could also be used if the resulting potential profile is smooth on the length scale of l .

III. SCREENING RESULTS

In this section we present our results calculated within the self-consistent scheme, starting by discussing the zero temperature, zero magnetic field limit and then compare the obtained density profiles with the finite temperature and field profiles. The aim of this investigation is to clarify the effect of the quantizing perpendicular magnetic field, which introduces local charge imbalances due to formation of the ISs. We have already argued that the electron density distribution is highly sensitive to the applied external magnetic and electric fields. Therefore even very small changes in these external parameters affect the density and potential profiles drastically.

It is shown^{26,27,41} that the formation of the compressible and ISs results in an inhomogeneous density distribution that deviates from the zero field profile. This deviation creates a local charge imbalance generating a potential fluctuation. We describe this fluctuation by

$$\Delta V(x) = [V(x,0,0) - V(x,T,B)]/\Omega_2, \quad (18)$$

where the self-consistent potentials are calculated at zero and finite magnetic field and temperature, respectively [see Fig. 4(b)]. Hereafter $\Omega_2 (= \hbar \omega_c / E_0 = 0.328 \times 10^{-2})$ represents the dimensionless cyclotron energy at average filling factor 2, since we always consider situations where average filling factor is around 2. We start our analysis by discussing the effect of the local charge deviation from its equilibrium distribution at $T=0, B=0$. Figure 4(a) depicts the electron densities calculated within the SCTFPA for vanishing and finite magnetic field and temperature, where we used 300 mesh points to span a single layer. The curves for finite field and temperature show a considerable deviation from the curves for zero field and temperature in the intervals ($200 \text{ nm} < |x| < 1000 \text{ nm}$), where one observes ISs at the top layer. In the inset we concentrate on this interval. In Fig. 4(a) we compare the $T=0, B=0$ density curves to the $T \neq 0, B \neq 0$ ones. In the interval $-600 \text{ nm} < x \leq -300 \text{ nm}$ there are less electrons at the top layer due to the formation of an IS. This yields a less repulsive interlayer Coulomb interaction; so that more electrons are populated locally at the bottom layer. Similar arguments hold for the left-hand side of the IS ($-800 \text{ nm} \leq x < -600 \text{ nm}$), however, now the potential becomes more repulsive and thus more electrons are depleted from the bottom layer locally. The corresponding potential variations are shown in Fig. 4(b), the peaklike behavior near the edges results from temperature difference, whereas the

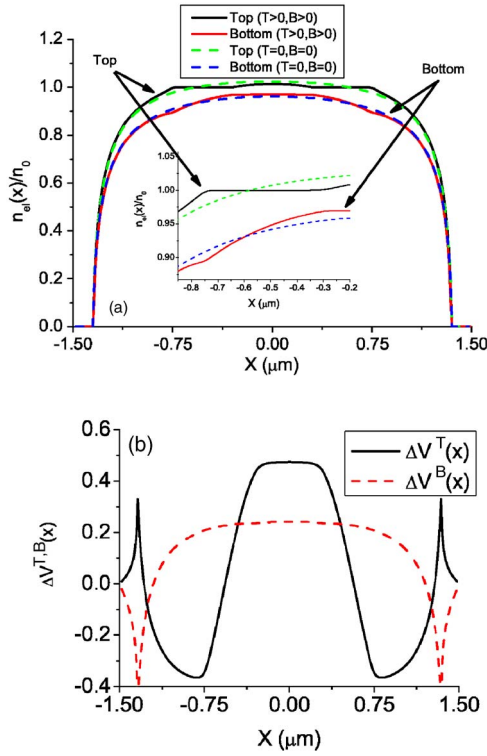


FIG. 4. (Color online) (a) Electron densities for a finite magnetic field (such that $\bar{\nu}_{av}^{tot}=1.6$) and at default temperature ($kT/E_0=5 \times 10^{-5}$ or $kT/E_F \sim 0.01$), for top and bottom (thin solid-line) layers; also for vanishing field and temperature (dotted lines). (b) The resulting potential variation due to the formation of the ISs, where the superscripts refers to top (T) and bottom (B). The depletion length is set to be 150 nm and the density mismatch is governed by applying a finite gate potential $V_0/E_0^*=0.02$, resulting in $\bar{n}_{el}^T=3.42 \times 10^{11} \text{ cm}^{-2}$ and $\bar{n}_{el}^B=3.18 \times 10^{11} \text{ cm}^{-2}$. The inset shows the region where an IS exists at the top layer.

structure observed at the top layer is due to the formation of the IS in the same layer. Since the bottom layer is completely compressible the potential variation does not show any non-monotonous feature and the fluctuation is perfectly screened. A relatively large variation is seen within the depletion regions. The reason for this is that, at finite temperature the density profiles leak out at the edges. At very strong magnetic fields [$\nu(0) < 2$] only the lowest Landau level is partially occupied, i.e., high DOS, thus the density profiles for vanishing and for very strong magnetic field should look very similar. However, for intermediate B there is a difference due to the quantizing magnetic field that creates dipolar (incompressible) strips at the top layer, which have an influence on the bottom layer via the strong Coulomb interaction. Therefore it is essential to examine the formation of the ISs at strong magnetic fields. This is done by manipulating the sheet electron densities by applying a finite gate bias. The gate controls the existence and positions of the ISs indirectly, so that one can examine the screening effects of the ISs considering the electron density distributions. In the later sections, potential fluctuations created by these local charge imbalances, i.e., the ISs, will be connected to the magnetotransport quantities, where we explicitly show the impact of the ISs on the Hall resistances.

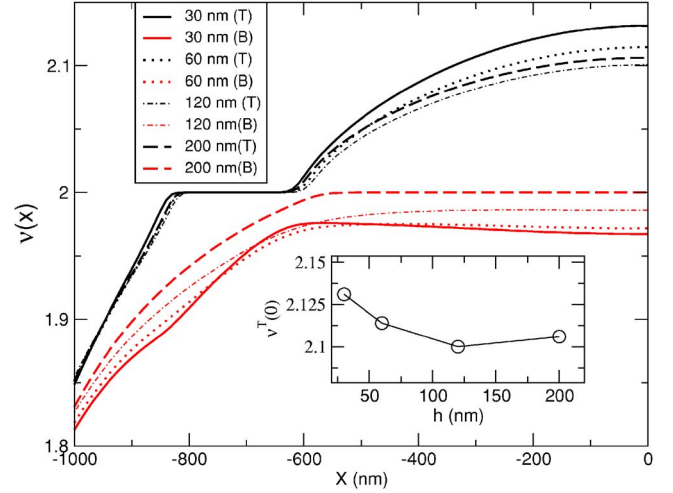


FIG. 5. (Color online) Local filling factors versus position at a finite magnetic field and for $h=30, 60, 120$, and 200 nm, at default temperature. The top layer (upper set) exhibits an IS, whereas the bottom layer (lower set) is compressible all over the electron channel, except $h=200$ nm. The inset depicts the center filling factor of the top layer for four h values.

A. Intralayer distance, temperature, and density mismatch

It is known that the mutual Coulomb interaction is a strong long-range interaction. Thus a change in the charge distribution, compared to the equilibrium distribution (at $T=0, B=0$), produces a considerable effect on the observable quantities even at large distances. In the previous section it is shown that such a local charge imbalance, connected with a potential fluctuation, is created due to formation of the ISs. Here we investigate the density distributions of the layers by applying a positive gate voltage, hence populating the top 2DES and vary the intralayer distance and temperature. The average total filling factor, $\bar{\nu}_{av}^{tot}=(\nu^T+\nu^B)/2$, is kept constant and the evolution of the ISs at the top layer, and its effect to the bottom layer, is examined. In Fig. 5 we show the local filling factors of both layers versus position, where the top layer (upper set of curves) has an IS in the interval $-850 \text{ nm} < x < -600 \text{ nm}$ for different interlayer distances. The influence of the IS in the top layer on the electron distribution of the bottom layer disappears rapidly although the intralayer distance is changed rather smoothly. This is due to exponential decay of the amplitude of the Coulomb potential in the z direction, i.e., $V(q, z) \sim V_q \exp(-q|z|)$. The effective confining potential (ECP) experienced by each layer, of course, depends strongly on the interlayer distance, hence for each h value the number of electrons at each layer changes. This is depicted in the inset of Fig. 5, there we concentrate to the center filling factor. We observe that by increasing h ($=30, 60$, and 120 nm) the number of electrons at the center decreases (at fixed magnetic field) and the ECP becomes less confining thus a flatter density distribution is observed. Interestingly, for the largest separation ($h=200$ nm) the bottom layer becomes widely incompressible at the bulk, hence semitransparent, and the electrons of the top layer start to see the donors of the bottom layer. This specific configuration leads accumulation of the top layer electrons to the bulk and

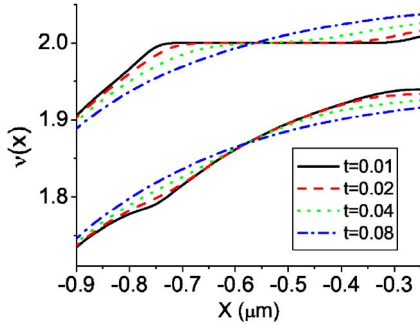


FIG. 6. (Color online) Local filling factor profiles across the sample concentrated to a region, where a IS resides at the top layer, for characteristic temperatures. The calculations are done at a fixed density mismatch, $\bar{n}_{cl}^B/\bar{n}_{cl}^T=0.93$, with $\bar{\nu}_{av}^{tot}=1.6$ and $h=15$ nm, considering the depletion length to be fixed, i.e., $|b/d|=0.1$.

is a clear indication of nonlinear screening, due to ISs, in such a bilayer system. This fact emphasizes that even a small change at h has a strong influence on the electron density profile. The exponential decay of the Coulomb interaction in the growth direction essentially determines whether the two 2DESs are strongly coupled or not, depending on the formation of the ISs, i.e., screening. In the relevant experiments the distance between the two layers is fixed during the growth process. Hence we proceed our investigation by fixing $h=15$ nm and vary the electron temperature. For such a separation the system is known to be electronically uncoupled and can be described by two electrochemical potentials.

In Fig. 6 the temperature dependence of the IS residing in the top layer and the compressible region at the bottom layer is shown. At single layer geometries it is well-known^{27,32} that the quantizing effect of the magnetic field becomes inefficient if the thermal energy of the system becomes larger than a few percents of the cyclotron energy. Here we also observe a similar behavior for the bilayer system where the IS at the top layer and, moreover, the local charge imbalance seen at the bottom layer disappears while increasing the dimensionless temperature $t(=kT/E_F)$ from 0.01 to 0.08. This fact

shows that the local inhomogeneity at the bottom layer density distribution is only due to the dipolar strip at the top layer and is very sensitive to the temperature and exists for $t < 0.04$. Relevant to the experiments considered, density mismatch is another tunable parameter, like the temperature. In order to investigate the effect of the density mismatch, now we fix the temperature and intralayer distance and vary the potential of the top gate essentially by changing the number of induced positive charges. Figure 7 presents position dependent filling factors for a positively charged gate, simulating different density mismatches by applying a gate bias voltage V_0 . For a slight mismatch one does not observe a prominent change, except more electrons are accumulated at the center of the top layer. Due to the stronger Coulomb repulsion the bulk of the bottom layer is more depopulated and shows a flatter profile [see Fig. 7(a)]. In Fig. 7(b), this feature is more pronounced at a higher gate bias and, in turn, the bottom layer is forced to be incompressible at the bulk, leading the effective external potential to be more confining for the top layer. The outer edge regions of ISs residing at the top layer suppress the electrons beneath, at the bottom layer. Increasing the density mismatch in favor of the top layer, in Figs. 7(c) and 7(d), it is observed that more electrons start to accumulate at the bulk of the top layer and small density fluctuations can be seen at the bottom layer, however, we do not see any prominent change at the density profiles since the bottom layer can screen perfectly. We close our short discussion by noting that even a small amount of density mismatch can lead to a drastic change in the density profiles. Moreover, this change is enhanced by the existence of the IS, which results from the nonlinear screening in the presence of external magnetic field. This high sensitivity to the external electric field (here the gate) is clearly seen if the potential profiles are considered. We shall emphasize that a wide IS formed at the bulk of one of the layers does not necessarily imply that this layer becomes completely transparent to its donors, since the electrons residing in the IS *also* create an electric field which can still partially cancel the electric field generated by its donors.

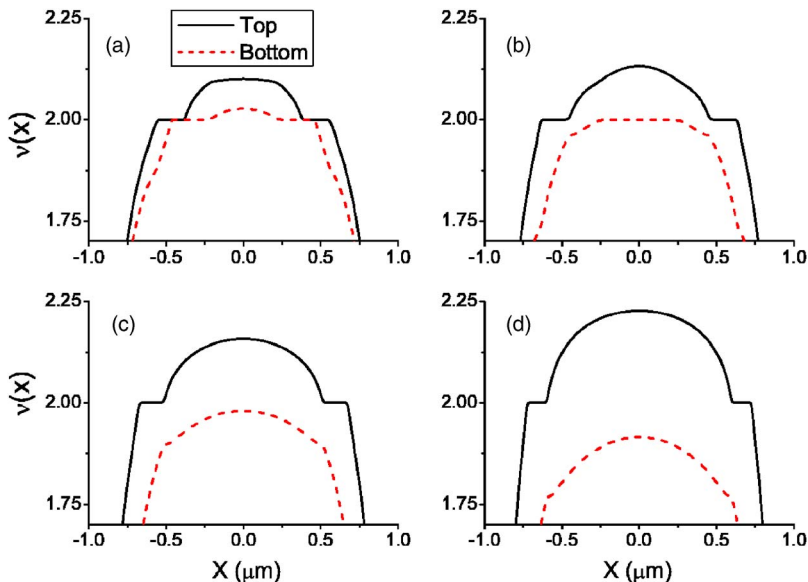


FIG. 7. (Color online) The top layer is populated by applying a finite gate potential V_0/E_0^* (a) 0.01, (b) 0.02, (c) 0.03, and (d) 0.05 corresponding to density mismatches of $\bar{n}_{cl}^B/\bar{n}_{cl}^T=0.96, 0.93, 0.89,$ and 0.84 , respectively. Given at default temperature, with the depletion length, $b/d=0.9$ and $\bar{\nu}_{av}^{tot}=1.67$.

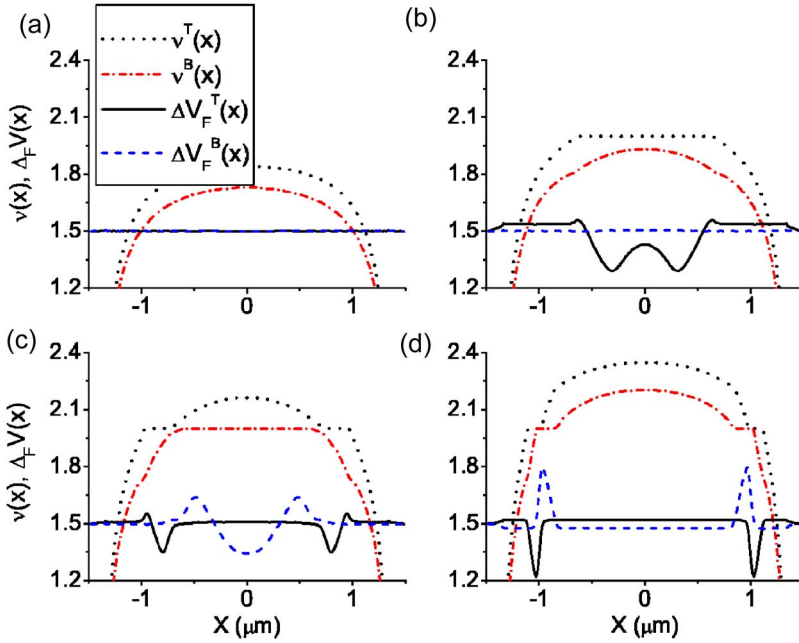


FIG. 8. (Color online) Position dependent filling factors and magnetic field induced potential variations, for $\bar{\nu}_{av}^{tot}$ (a) 1.44, (b) 1.59, (c) 1.69, and (d) 1.84. For clarity all the potential variations are shifted by an amount of 1.5. The gate potential is set to $V_g/E_0^* = 0.02$, for fixed depletion and at default temperature.

B. Potential fluctuations

In this section we examine the effects of the ISs residing in one layer, on the external potential profile of the other layer by comparing what we call the “interacting” and the “noninteracting” systems. In both cases we start with the self-consistent calculation of the density and potential profiles at $T=0$, $B=0$. Then we focus on one layer, bottom or top, which we call the “active” layer while the other layer is called the “passive” one. Now we keep the $T=0$, $B=0$ density and Hartree potential profile of the passive layer fixed and calculate in the corresponding, B -independent external potential of the active layer, its density, and potential profile self-consistently at finite T and B . This yields the total potential $V_N(x, z)$ of the noninteracting system. It takes into account the B -dependent intralayer screening properties in the active layer, but not the B -dependent changes of the intralayer screening in the passive layer and of the interlayer screening. Finally we drop the restriction on the passive layer and calculate density and potential profiles for both layers at finite T and B fully self-consistently. This yields the total potential $V_I(x, z)$ of the interacting system.

The potential variation (at finite temperature and magnetic field, indexed by F as a subscript)

$$\Delta_F V(x) = [V_I(x, z) - V_N(x, z)]/\Omega_2, \quad (19)$$

taken at the z value of the active layer, describes the B -dependent change of the interaction of the active with the passive layer. It is suitable for studying the effect of the ISs in the passive layer on the effective potential in the active layer. Figure 8 shows potential variation and filling factors across the sample at four different magnetic field values where the superscript T(B) indicates that the top (bottom) layer is the active layer. In Fig. 8(a) the magnetic field strength is chosen such that both layers are compressible, i.e., the center filling factors of both layers are slightly below 2. The potential variation shows a characteristic behavior as

the layers are both compressible all over the sample, the screening is nearly perfect, and we do not observe any significant potential fluctuation. If one decreases the magnetic field strength and obtains a wide IS in the bulk of the top layer [Fig. 8(b)], a large potential variation is observed at this layer. This is nothing but the charge quadrupole at the center, treated by Ref. 53 for a single layer geometry. The variation drastically increases and becomes almost $\sim 30\Omega_2\%$. Meanwhile, the variation of the bottom layer does not show any significant change. The explanation of these observations is twofold; first since an IS is formed at the top layer, the finite field density profile strongly deviates from the zero field profile, which essentially creates a huge local (within the IS) external potential fluctuation to the bottom layer. Second, the bottom layer is completely compressible, so that this large potential fluctuation can be screened by redistribution of the bottom layer electrons, resulting in a density deviation from the zero B profile. Note that as a consequence of the self-consistency the deviation is spread all over the bottom layer, which also generates an external potential fluctuation to the top layer. Here, since we examine how the top layer responds to this external potential fluctuation we remind the reader that there are two different regions with different screening properties: (i) The compressible regions [$0.5 \mu\text{m} < |x| < 1.5 \mu\text{m}$ interval in Fig. 8(b)] show similar features to the bottom layer and the external potential fluctuation is well-screened. (ii) The incompressible region [$0 \mu\text{m} < |x| < 0.5 \mu\text{m}$ interval in Fig. 8(b)] at the bulk can poorly screen the fluctuation and one observes that $\Delta_F V(x)$ can be as large as half the Fermi energy. In Fig. 8(c), the magnetic field strength is slightly decreased in order to obtain a wide IS at the bottom layer, meanwhile the wide IS of the top layer splits into two ribbons which are shifted towards the edges. For this B value, one observes both the quadrupole (for the bottom layer) and the dipole (at the top layer) moments. Figure 8(d) shows the case, where two well-developed ISs are present at both of the layers and the potential fluctua-

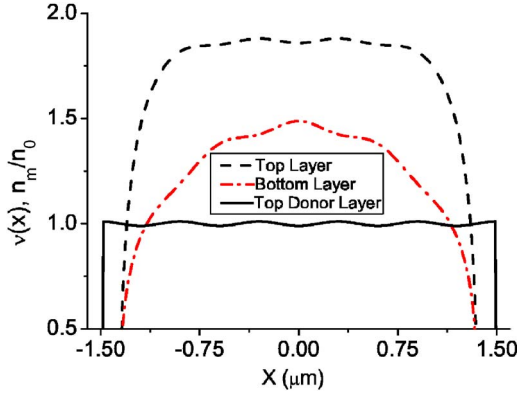


FIG. 9. (Color online) Spatial distribution of the donors (solid line), together with the local filling factors of top (dashes) and bottom (dash-dot) layers at default temperature.

tions, created by the charge dipoles, are confined to these regions. Different than the previous case we only observe one side of the dipole moment, since the other half is screened by the other layer. We should emphasize that the variation amplitude depends on the width of the IS which generates the fluctuation, since the charge imbalance becomes larger if the IS is wide. The finding is simply that the potential fluctuations in a layer exist only within incompressible regions and are screened in compressible ones.

C. Modulated donor distribution

It is rather a common technique to add an external (harmonic) modulation potential to the confinement potential in order to study the peculiar low-temperature screening properties of a 2DES, which has been done for single layer geometries.^{31,41,54} Although a double layer geometry is a very promising system, even a qualitative investigation of such a modulation is still missing in the literature. In this section we provide a simple model to discuss the effect of

this modulation on screening and compare our results, qualitatively, with the single layer ones.

A harmonic density modulation is added to the background charge distribution to obtain a potential modulation. Here we should also note that such a modulation will be used to simulate the long-range fluctuations of the confining potential in the following sections,³⁵ meanwhile the SR part will be included to the conductivity model. It is assumed that the spatial distribution of the donors is given by

$$n_m(x) = n_0\{1 - \delta \cos[\lambda \pi(x/2d)]\}, \quad (20)$$

where λ is an odd integer preserving the boundary conditions and δ describes the strength of the modulation. In the following discussion we will fix the density mismatch, $\bar{n}_{el}^B/\bar{n}_{el}^T = 0.77$, modulation period, $\lambda = 11$, temperature, $t = 0.01$, and the average filling factor, $\bar{\nu}_{av}^{tot} = 1.34$, to calculate the electrostatic quantities. We see in Fig. 9 that the top layer is in phase with the modulation, whereas the bottom layer's phase is shifted by an amount of $\pi/2$, where the modulation strength is chosen to be 1%. For the given parameters both layers are compressible and screening is still linear [see Fig. 10 region (i)], i.e., the electrons can redistribute according to the applied external potential. A similar case for single layer geometries has been extensively studied in Refs. 41 and 54, the momentum (q) dependent dielectric function is given by $\epsilon(q) = 1 + 1/a_0q$ (~ 19 for our parameters). This linear screening approximation breaks down when the amplitude of the screened potential becomes equal to the Fermi energy of the unmodulated system.⁵⁵ From this we would expect that the breakdown amplitudes of the two layers should be directly proportional to the density mismatch. In order to test this and examine the nonlinear screening regime we increase the strength of the modulation monotonously and look at the variation of the screened potential defined by

$$\text{var}[V^{T,B}] = V^{T,B}(x=0) - V^{T,B}(x=0.3 \mu\text{m})/\Omega_2. \quad (21)$$

Figure 10(a) presents this variation, for top (solid line) and bottom (dashed line) layers. In the regime denoted by (i)

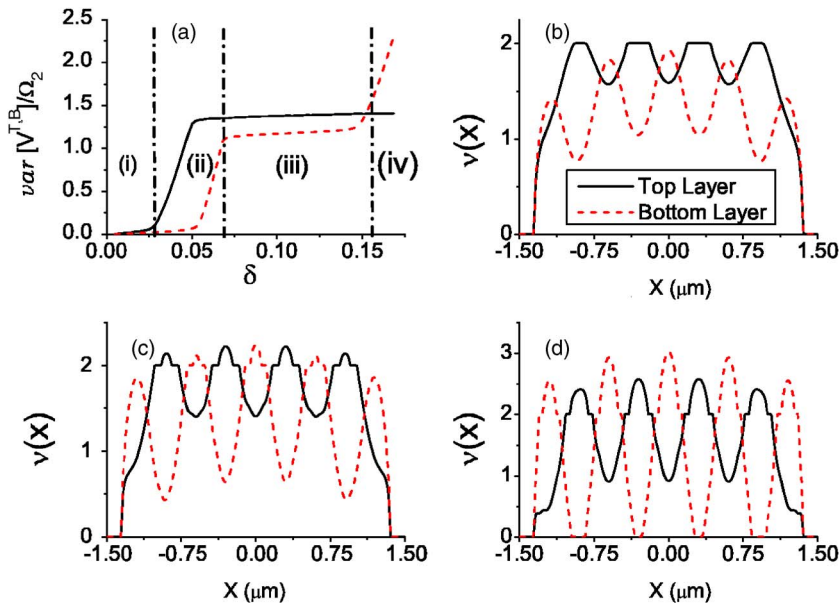


FIG. 10. (Color online) (a) The variation of the screened potential versus the modulation amplitude, together with the typical electron densities corresponding to different screening regimes (b) ii, $\delta = 0.026$, (c) iii, $\delta = 0.073$, and (d) iv, $\delta = 0.157$. For top (solid lines) and bottom (dashed lines) layers.

both layers are compressible and the density profile can be characterized similar to Fig. 9. With increasing the modulation amplitude first the top layer enters the nonlinear screening regime, since ISs are formed [see Fig. 10(b)]. This is pronounced as a jump in the variation and saturates at $\delta \sim 0.05$ [regime (ii)], meanwhile the bottom layer is still compressible (i.e., in the linear regime) and compensates (screens) the potential fluctuation generated [cf. discussion related to Fig. 8(b)]. From the saturation point we can easily predict the similar point of the bottom layer to be $\delta \sim 0.07$. Actually we see that regime (iii) of Fig. 10(a) starts at the expected value, where ISs are present at both layers showing a characteristic distribution similar to Fig. 8(c). Here screening becomes linear again, but now with $\epsilon(q) = 1 + (D_T/D_0)/(a_0q)$, where D_T is the thermodynamic DOS in a Landau level, which can be estimated by $D_T/D_0 \sim \hbar \omega_c / (4k_B T)$. For $\delta > 0.15$ the bottom layer is split to five narrower channels [see Fig. 10(d)] and the linear screening is broken around $\delta \sim 0.16$. From the analytical expressions given in Ref. 54 one can estimate the breakdown amplitude as

$$\delta_{bd} \sim \frac{2E_F^B \epsilon(q)}{E_0} \sim 0.16, \quad (22)$$

which indeed is in very good agreement with the obtained numerical result. The small difference is due to the higher temperature and the decay of mutual Coulomb interaction in growth direction, likewise the difference at the slope of the plateaus. We also observe that the plateaus occur at the integer multiples of the individual filling factors, similar to the single layer system. Since we start with a situation where the average filling factors of both layers are below two we see only one plateau, as discussed for the single layer geometries the number of the plateaus depends on the average filling factor without modulation. Finally we would like to note that the linear screening will break down for the top layer for $\delta \sim 0.2$ which can be seen easily from Eq. (22). The potential fluctuations and the donor modulation discussed above plays an important role when one considers a fixed external current flowing through both of the layers. These fluctuations are generated by local charge imbalances, with respect to zero field density distributions, and can be observed in the interval where the other layer has an IS as they are poorly screened.

IV. THE HALL RESISTANCE CURVES

In this section we investigate the effects of potential fluctuations on the Hall resistances using the findings of Guven and Gerhardt's (GG)³³ and SG,²⁹ within the linear response regime, which we next summarize briefly.

In their work, from the equation of continuity and the Maxwell's equations (with the assumption of translational invariance), it was found that the current density across the Hall bar vanishes, i.e., $j_x(x) = 0$, and the electric field along the sample is a constant ($E_y = E_y^0$). Meanwhile, the current density (position dependent) along and the Hall field across the sample is given by

$$j_y(x) = E_y^0 \rho_l(x), \quad E_x(x) = E_y^0 \rho_H(x) / \rho_l(x), \quad (23)$$

which is determined by the longitudinal ($\rho_l = \rho_{xx} = \rho_{yy}$) and the Hall ($\rho_H = \rho_{xy} = -\rho_{yx}$) components of the resistivity tensor

$$\hat{\rho}(x) = [\hat{\sigma}(x)]^{-1} = \frac{1}{\sigma_l^2(x) + \sigma_H^2(x)} \begin{bmatrix} \sigma_l(x) & -\sigma_H(x) \\ \sigma_H(x) & \sigma_l(x) \end{bmatrix}. \quad (24)$$

Considering a fixed imposed current $I = \int dx j_y(x)$, one can obtain the position dependent chemical potential for each layer, $\mu_{T,B}^*$, from the above equations. They have found that, for sufficiently low currents (linear response regime) the current-induced changes of the electrostatic potential within the 2DES practically agree with the current-induced changes of the chemical potential.³³

It can be seen from Eqs. (23) and (24) that any reasonable conductivity model with well-separated LLs at low temperatures, at (even) integer filling factors ($\nu = 2k$) yields

$$\rho_l = \sigma_l = 0, \quad \rho_H = 1/\sigma_H = h/(e^2 2k), \quad (25)$$

and no elastic scattering is possible. Therefore in the presence of an IS with a finite width, the $1/\rho_l(x)$ will be infinite. Integrating $j_y(x)$ and $E_x(x)$, for a fixed and finite I , one observes that in the limit $T \rightarrow 0$ the only contribution comes from the ISs and the electric field vanishes. If only ISs with local filling factor $\nu = 2k$ exist, one immediately sees from Eq. (23) that the Hall voltage $V_H = \int dx E_x(x)$ is the $h/(e^2 2k)$ -fold of the current, so that the Hall resistance

$$R_H = V_H/I = h/(e^2 2k) \quad (26)$$

is quantized, while the longitudinal resistance

$$R_l \propto E_y^0/I \quad (27)$$

vanishes. At zero temperature the quantization is *exact*, at low temperatures the corrections are exponentially small. In the case of no ISs the resistances are defined by the details of the conductivity model.

As promised before, we now discuss shortly the effect of the disorder on the DOS, within the SCBA. The well-established wisdom is that, without any impurities it is not possible to define a finite longitudinal conductivity. The SCBA⁵⁰ assumes that the Coulombic impurities introduced by the donors can be represented as Gaussians and in turn the spectral function can be expressed as

$$A_n(E) = \frac{2}{\pi \Gamma_n} \sqrt{1 - \left(\frac{E - E_n}{\Gamma_n} \right)^2}, \quad (28)$$

where Γ_n 's define the widths of the broadened DOS (for a detailed derivation cf. Ref. 56 or for a short review, the appendix of Ref. 29). Starting from Eq. (28), one can calculate the collision broadened DOS and the entries of the conductivity tensor for given sample parameters. At the present work we will use the results of SCBA for intermediate range ($R \sim l$ and $\Gamma/\hbar \omega_c = 0.01$) of the single impurities and include the LR part of the disorder potential to the confining potential as done in Sec. III C. Since the broadening of the DOSs is smaller than the thermal window $k_B T$, the effect of colli-

sion and exchange, mentioned while discussing ECEs, broadening has essentially no effect on the screening calculations, however, it is enough to obtain a finite σ_l . We should mention that in the work of GG other DOS models were also investigated, e.g., Gaussian and Lorentzian broadening for the DOS and even a simpler model to define the σ_l ,⁵⁷ yielding similar results on the conductivity, although the details of the model effect the widths of the ISs quantitatively.

A final remark on the (long-range) potential fluctuations resulting from the disorder is that they can widen, stabilize, and shift the quantized Hall (QH) plateaus as they affect the position and the existence of the ISs.³⁵ In addition to the LR fluctuations due to the donors, in this section we also include the potential fluctuations generated by the local charge imbalances, namely generated by the ISs shown in Sec. III B. Here we use the expressions given by Eqs. (23)–(27), for a given electron density and fixed current, to calculate the Hall and longitudinal resistances of the bilayer system. A simple way to improve on the strictly local conductivity model is to replace the conductivity tensor by its spatial average (λ_{av}) taken over the order of mean electron distance (i.e., the Fermi wavelength) as done before.^{29,39} In particular λ_{av} is set to be 40 nm in our calculations, which is essentially the Fermi wavelength. With this improvement and a consistent model for conductivity and collision broadening of the Landau levels we calculate in the linear response regime for the the interacting and noninteracting systems the MR curves. We remind that, in the case of a noninteracting system, the active layer does not have information about the density inhomogeneities caused by the ISs of the passive layer. Hence comparing the resistance curves of these two cases essentially gives a method to extract the effect of the ISs on the other layer.

In order to investigate the relation between the ISs of the passive layer and the magnetotransport coefficients of the active layer qualitatively, we calculate the Hall resistances for a magnetic field interval, where QH plateaus are observed for both layers around filling factor 2. In Fig. 11 we show the Hall resistances (in units of the von Klitzing constant) vs magnetic field for interacting (solid lines) and noninteracting (dashed lines) systems. We start the discussion with the high-magnetic field regime ($\Omega_c/\Omega_2 > 1.27$, i.e., right side of the vertical dotted line), which essentially corresponds to a density distribution similar to that shown in Fig. 8(a). Since there are no ISs within both layers, no noticeable potential fluctuations are created due to local charge imbalance, therefore the Hall resistances of both layers are the same for interacting and noninteracting cases. If we examine the QH regime of the top layer (the regime between vertical dash-dotted line and dotted line in Fig. 11), it is seen that at least one IS is formed [cf. Fig. 8(b)], creating a potential fluctuation to the bottom layer. Meanwhile, the bottom layer is still compressible all over the sample, so the fluctuation can be screened nearly perfect, leading to a new distribution of the electrons and a small change in the R_H curves, due to the rearrangement of the local conductivities. The situation is fairly different, in the interval $1.18 < \Omega_c/\Omega_2 < 1.25$ (the region between the thin vertical solid line and dashed-dotted line), where ISs are formed at both of the layers (density distributions corresponding to Figs. 8(c) and 8(d)]. In this

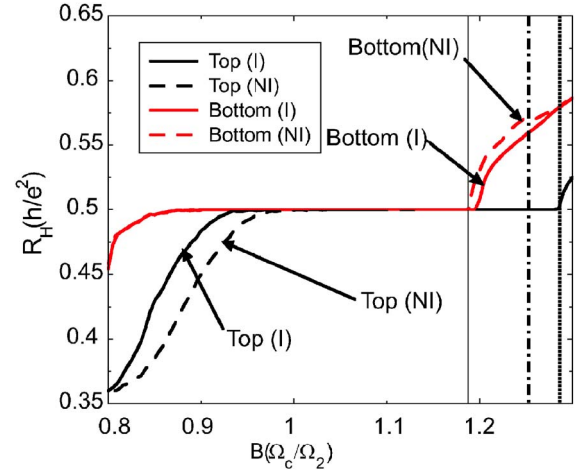


FIG. 11. (Color online) Comparison of the interacting (solid lines) and noninteracting (dashed lines) Hall resistance curves for fixed electron densities at default temperature. The Hall resistance curve is shifted for the top layer as the potential fluctuation created by the bottom layers IS.

regime, both layers produce fluctuations due to local charge imbalance and this fluctuation cannot be screened perfectly everywhere, which in turn results in a difference in the Hall resistance curves. This is observed for the bottom layer at the high-magnetic field edge, since the perturbation slightly shifts the maximum magnetic field value of the QH plateau. In this regime the quantized value of the Hall resistance of the top layer does not change, since it only depends on the presence of the IS [cf. Eq. (26) and the related text]. In the $1 < \Omega_c/\Omega_2 < 1.18$ interval of Fig. 11 there exists two stable ISs in both layers surrounded by compressible regions, thus both layers are in the QH plateau. Here we should note that, although the potential fluctuations are created by the ISs and are not screened perfectly, this perturbation changes only the positions or the widths of the ISs, but not the value of the R_H within the plateau regime. Eventually it depends on the amplitude of the perturbation, i.e., if the amplitude is large enough to destroy the ISs one does not observe the quantized value for R_H . The change in R_H can be observed for the top layer at somewhat smaller values of the magnetic field strength ($0.8 \leq \Omega_c/\Omega_2 \leq 1.0$) since the perturbation enlarges the plateau. In fact the fluctuation widens the ISs with respect to the noninteracting case and creates ISs larger than the averaging length, λ_{av} . Finally one ends with a wider plateau. The difference in the Hall resistance curves between the interacting and noninteracting systems tends to disappear since the ISs become narrower and move towards the edges by decreasing the magnetic field. This is consistent with the previous observation that the amplitude of the fluctuation depends on the width of the incompressible region.

In summary four magnetic field intervals are observed: (i) both layers are compressible and there exists no difference for the R_H curves, calculated for the interacting and noninteracting case; (ii) the top layer, at least, has an IS which creates a fluctuation, and the edge of the Hall plateau is shifted to a higher B value for the bottom layer; (iii) both layers show incompressible regions, the perturbation gener-

ated by the bottom layer widens the ISs of the top layer, leading to a wider plateau; and (iv) the ISs of both layers become narrower and move towards the edges and the fluctuation becomes inefficient, hence the difference is smeared out. It is useful to mention that the *interacting* system is an *equilibrium* solution, in the sense that the electrons of both layers rearrange their distribution until a full convergence is obtained (within a numerical accuracy), for a given external potential profile.

In the next section we concentrate on a characteristic result of the measured MR hysteresis. Different from our previous work we confine our interest to the difference between the “interacting” and “noninteracting” cases. There, we attempt to establish the analogy between the hysteresis and the plateau widening, without using the frozen density/potential model.

V. COMPARISON TO THE EXPERIMENTS

Here we report on the magnetotransport hysteresis observed in the bilayer systems measured at the Max-Planck Institut-Stuttgart by Kraus.³⁹ In the experiments discussed here, the MRs are measured as a function of the applied perpendicular magnetic field. The sweep direction dependence is investigated for a certain density mismatch. Similar findings have already been presented in the literature,^{17–20,39} however, they have been discussed in a different theoretical content. In particular, in Ref. 39 the hysteresis is attributed to the thermodynamic nonequilibrium and it was shown that by the reestablishment of the equilibrium (by warming up the sample in each sweep step) the hysteresis disappears. In the present work, we concentrate ourselves to the effects of local charge imbalances generated by the ISs (Sec. III B) and relate the widening of the QH plateaus (Sec. IV) with the hysteresis.

The samples are GaAs/AlGaAs double quantum well structures grown by molecular beam epitaxy (MBE). Separate ohmic contacts to the two layers are realized by a selective depletion technique.⁵⁸ An important note about the realization of the separate contacts is that it rules out the possibility to explain the observed hysteresis by means of charge transfer via the ohmic contacts, which was proposed earlier by Pan *et al.*^{19,20} A technique developed by Rubel *et al.*⁵⁹ was used to fabricate backgates. The metal gate on top of the sample acts as a frontgate. The samples were processed into 80 μm wide and 880 μm long Hall bars. The high mobility samples are grown at the Walter-Schottky Institut. They have as grown densities in the range $(1.5\text{--}2.5) \times 10^{11} \text{ cm}^{-2}$ and mobility is 100 $\text{m}^2/\text{V s}$ per layer. The barrier thickness is 12 nm and the quantum wells are 15 nm wide. The experiments were performed at low temperatures ($T \approx 270 \text{ mK}$) and the imposed current is always in the linear response regime ($I \sim 50 \text{ nA}$). Other details of the experimental setup and samples can be found in Ref. 39.

We show the measured Hall resistances of the top layer [solid dark (black) lines for up and dotted (black) lines for down sweep] and the bottom layer [solid light (red) lines for up and dotted light lines for down sweep] as a function of magnetic field strength and direction in Fig. 12. The data

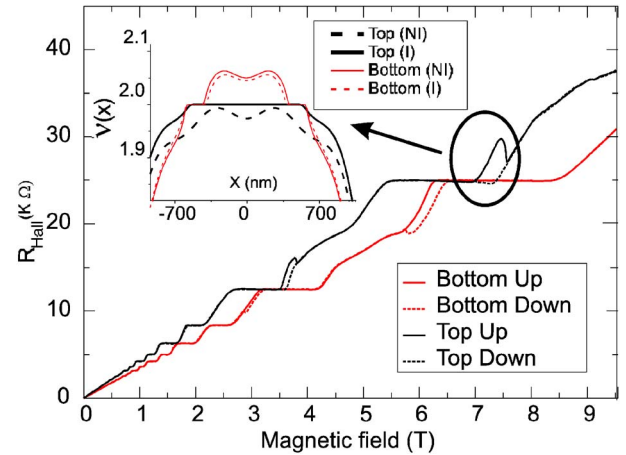


FIG. 12. (Color online) The Hall resistances as a function of magnetic field for a GaAs electron bilayer system with a barrier width 12 nm, considering two sweep directions. Data is taken at a magnetic sweep rate 0.01 T/min. A strong hysteresis develops in R_H when the other layer is in a plateau. No significant effect is observed at low field regime. The inset depicts the local filling factors for top (thick lines) and bottom (thin lines) layers calculated with interaction (solid lines) and without interaction (broken lines).

were taken at a sweep rate 0.01 T/min and the base temperature is always kept at 270 mK. Apparently it is seen that the resistances of the layers follow different traces depending on whether the sweep is in up or down direction, in certain B field intervals. We see that the sweep direction has no effect on the resistances at high magnetic fields ($B > 8 \text{ T}$), where we would not expect²⁹ to have any ISs [see, e.g., Fig. 8(a)]. The first exiting feature is observed when the bottom layer is in the plateau regime and the top layer is approaching its plateau regime ($6.5 \text{ T} < B < 8.1 \text{ T}$). It is seen that the Hall resistance of the top layer follows two different traces depending on the sweeping direction, meanwhile the bottom layers resistance is insensitive and assumes the quantized value.

The plateau regime is extended up to $B \sim 7.25 \text{ T}$ for down sweep and ends at $B = 7 \text{ T}$ for up sweep, meanwhile the bottom layer is also in the QH regime. It is easy to understand why the QH regime is wider for the down sweep considering the widths of the ISs as follows: while coming from high magnetic field to low fields we first encounter a wide incompressible region at the bottom layer [see, e.g., the inset, comparing the interacting and noninteracting cases for the top layer, or equivalently Fig. 8(b), of course here the bottom layer has a higher density for the unmodulated system] that generates a large potential fluctuation yielding a wide plateau. However, for the other sweep direction two narrow ISs are observed first [Fig. 8(d)], which creates relatively weak fluctuations that have a negligible effect on the plateau width. For smaller values of the magnetic field, we observe at the top layer that up and down sweep curves follow the same trace and have the quantized value at $B = 6.8 \text{ T}$. A similar hysteresis behavior is seen at the bottom layer resistance curves ($5.7 \text{ T} < B < 6.5 \text{ T}$), now the top layer is in the plateau regime for both sweeping directions. The resistances at low magnetic field interval ($4 \text{ T} < B < 7 \text{ T}$) do not show a

prominent difference for two sweep directions. A less pronounced repetition of the hysteresis is observed at the $\nu=2$ plateau regimes, e.g., $3.4 \text{ T} < B < 3.6 \text{ T}$ and $2.9 \text{ T} < B < 3.2 \text{ T}$. A common feature (also observed at different density mismatches) is that the hysteresis is seen at the active layer only if the passive layer is in the plateau regime. No hysteresis is observed if the QH regimes of the layers coincide (see discussion in Ref. 39). We summarize the experimental observations as follows: the hysteresis is observed in the active layer only if the passive layer is in the plateau regime. The inset shows a possible local filling factor distribution in the regime where the bottom layer is already in the plateau and it starts to set in for the top layer (the region denoted by the black ellipse). One can see that both for interacting and noninteracting calculations well-developed ISs exist at the bottom layer, therefore we do not observe any difference in the MR curves for the bottom layer. The quantized value is a direct consequence of Eq. (26). For the top layer the case is quite different: if the interaction is allowed between the layers at finite B , the ISs at the bottom layer create potential fluctuations to the top layer, thus the top layer also enters to the QH regime at a high B value compared to the noninteracting case. In the absence of the potential fluctuations, i.e., the noninteracting case, the plateau regime for the top layer sets in for a lower B field strength. Similar arguments hold for the bottom layer in the opposite case, where the potential fluctuations widen the plateau from the low B field edge. A short remark would be that, during the up sweep one always starts with two narrow ISs at the edges, thus the two layers interact strongly, whereas during the down sweep the large IS formed at the bulk of one of the layers suppresses the (intra- and inter-layer) interaction, therefore equilibrium. The fact is that the simulation of the nonequilibrium by frozen density/potential profiles can be justified under this circumstance, which was done before in our previous work.³⁹

We should mention that the hysteresis effect is a nonequilibrium effect and the “interacting” system is an equilibrium solution, and hence cannot explain this effect directly. However, it is easy to attribute the widening of the top layers plateau (for down sweep) to the potential fluctuations created by the bottom layer, as already shown for the “interacting” case in Fig. 11. In accordance with our numerical results (previous section) obtained for the “noninteracting” system, the measured quantities are independent of their history. We claim that the measured resistances are the analog of the calculated resistances for the noninteracting system for the up sweep of the top layer, since the ISs are narrow and the potential fluctuations are ineffective. Hence one cannot observe a significant effect on the MR curves.

VI. SUMMARY

In this work we have studied the screening properties of an e - e bilayer system. The electrostatic part is solved numerically using a self-consistent screening theory by exploiting the slow variation of the confining potential. We compared the electron distributions for vanishing magnetic field and temperature with the finite ones, and observed that a local charge imbalance is created due to the formation of ISs. These dipolar strips produce external potential fluctuations, as a function of applied magnetic field, to the other layer. We have investigated properties of this potential fluctuation by comparing the interacting and noninteracting systems for a few characteristic B values and obtained the Hall resistances by a local scheme proposed in our recent work.²⁹ We considered these fluctuations as a perturbation to the other layer and observed that they widen, stabilize, and shift the plateaus as expected. In Sec. V we have reported and attempted to obtain qualitative arguments for the hysteresislike behavior by reconsidering the symmetry breaking of the sweep direction, based on the long relaxation times of the incompressible regions. This is done by considering the “interacting” and “noninteracting” schemes. Our results show that the Hall resistance curves follow different paths if both of the layers have ISs within the sample. The amplitude of the deviation depends on the widths and the positions of the incompressible regions.

A further improvement of the existing model, which also reveals the out of linear response regime, may be helpful to grasp the underlying physics of the Coulomb drag experiments.³⁻⁸ Our preliminary calculations show that due to high current driven from the active layer the LLs of this layer are tilted, hence the electron densities, resulting in a considerable change of the passive layers electron density, which may be related to the drag effect. We believe that a similar approach of Zozoulenko *et al.*⁴⁵ to the ECEs within the LSDA+DFT is possible for the investigated system, which may also lead to investigation of the spin degree of freedom of strongly coupled bilayer systems, including the ones where an excitonic Bose-Einstein condensate is reported to be measured.⁶⁰⁻⁶²

ACKNOWLEDGMENTS

I would like to thank S. Kraus, S. C. J. Lok, W. Dietsche, and K. von Klitzing for their discussions and providing the experimental data. I am indebted to R. R. Gerhardts for many valuable criticisms and suggestions and also to S. Mikhailov for the initial discussions. During the refereeing process the suggestions helped to improve the paper, therefore I would also like to thank the referees. This work was supported financially by the Max-Planck-Institute FKF Stuttgart, SFB 631 and the German-Israel Project (DIP).

- ¹K. v. Klitzing, G. Dorda, and M. Pepper, *Phys. Rev. Lett.* **45**, 494 (1980).
- ²P. J. Price, *Physica B & C* **117**, 750 (1983).
- ³T. J. Gramila, J. P. Eisenstein, A. H. MacDonald, L. N. Pfeiffer, and K. W. West, *Phys. Rev. Lett.* **66**, 1216 (1991).
- ⁴U. Sivan, P. M. Solomon, and H. Shtrikman, *Phys. Rev. Lett.* **68**, 1196 (1992).
- ⁵N. P. R. Hill, J. T. Nicholls, E. H. Linfield, M. Pepper, D. A. Ritchie, A. R. Hamilton, and G. A. C. Jones, *J. Phys.: Condens. Matter* **8**, L577 (1996).
- ⁶H. Rubel, A. Fischer, W. Dietsche, K. von Klitzing, and K. Eberl, *Phys. Rev. Lett.* **78**, 1763 (1997).
- ⁷X. Feng, H. Noh, S. Zelakiewicz, and T. J. Gramila, *Bull. Am. Phys. Soc.* **42**, 487 (1997).
- ⁸J. P. Eisenstein, L. N. Pfeiffer, and K. W. West, *Bull. Am. Phys. Soc.* **42**, 486 (1997).
- ⁹A. P. Jauho and H. Smith, *Phys. Rev. B* **47**, 4420 (1993).
- ¹⁰H. C. Tso and P. Vasilopoulos, *Phys. Rev. B* **45**, 1333 (1992).
- ¹¹L. Zheng and A. H. MacDonald, *Phys. Rev. B* **48**, 8203 (1993).
- ¹²B. I. Halperin, P. A. Lee, and N. Read, *Phys. Rev. B* **47**, 7312 (1993).
- ¹³S. Sakhi, *Phys. Rev. B* **56**, 4098 (1997).
- ¹⁴M. C. Bonsager, K. Flensberg, Ben Yu-Kuang Hu, and A. P. Jauho, *Phys. Rev. B* **56**, 10314 (1997).
- ¹⁵F. von Oppen, S. H. Simon, and A. Stern, *Phys. Rev. Lett.* **87**, 106803 (2001).
- ¹⁶J. Zhu, H. L. Stormer, L. N. Pfeiffer, K. W. Baldwin, and K. W. West, *Phys. Rev. B* **61**, R13361 (2000).
- ¹⁷E. DePoortere, E. Tutuc, R. Pillarisetty, S. Melinte, and M. Shayegan, *Physica E (Amsterdam)* **20**, 123 (2003).
- ¹⁸E. Tutuc, R. Pillarisetty, S. Melinte, E. P. DePoortere, and M. Shayegan, *Phys. Rev. B* **68**, 201308(R) (2003).
- ¹⁹W. Pan, J. L. Reno, and J. A. Simmons, *Int. J. Mod. Phys. B* **18**, 3671 (2004).
- ²⁰W. Pan, J. L. Reno, and J. A. Simmons, *Phys. Rev. B* **71**, 153307 (2005).
- ²¹B. Kramer, S. Kettemann, and T. Ohtsuki, *Physica E (Amsterdam)* **20**, 172 (2003).
- ²²M. Büttiker, *Phys. Rev. Lett.* **57**, 1761 (1986).
- ²³S. Datta, in *Electronic Transport in Mesoscopic Systems* (Cambridge University Press, Cambridge, England, 1995).
- ²⁴E. Ahlswede, P. Weitz, J. Weis, K. von Klitzing, and K. Eberl, *Physica B* **298**, 562 (2001).
- ²⁵E. Ahlswede, J. Weis, K. von Klitzing, and K. Eberl, *Physica E (Amsterdam)* **12**, 165 (2002).
- ²⁶D. B. Chklovskii, B. I. Shklovskii, and L. I. Glazman, *Phys. Rev. B* **46**, 4026 (1992).
- ²⁷J. H. Oh and R. R. Gerhardt, *Phys. Rev. B* **56**, 13519 (1997).
- ²⁸T. Suzuki and T. Ando, *J. Phys. Soc. Jpn.* **62**, 2986 (1993).
- ²⁹A. Siddiki and R. R. Gerhardt, *Phys. Rev. B* **70**, 195335 (2004).
- ³⁰S. Ihnatsenka and I. V. Zozoulenko, *Phys. Rev. B* **73**, 075331 (2006).
- ³¹U. Wulf, V. Gudmundsson, and R. R. Gerhardt, *Phys. Rev. B* **38**, 4218 (1988).
- ³²K. Lier and R. R. Gerhardt, *Phys. Rev. B* **50**, 7757 (1994).
- ³³K. Güven and R. R. Gerhardt, *Phys. Rev. B* **67**, 115327 (2003).
- ³⁴A. Siddiki and R. R. Gerhardt, *Int. J. Mod. Phys. B* **18**, 3541 (2004).
- ³⁵A. Siddiki and R. R. Gerhardt, cond-mat/0608541, *Int. J. Mod. Phys. B* (to be published).
- ³⁶S. Kanamaru, H. Suzuura, and H. Akeru, *J. Phys. Soc. Jpn.* **75**, 064701 (2006); *Proceedings EP2DS-14*, Prague, 2001 (unpublished).
- ³⁷A. Yacoby, T. A. Fulton, H. F. Hess, L. N. Pfeiffer, and K. W. West, *Physica E (Amsterdam)* **20**, 65 (2003).
- ³⁸S. Ilani, J. Martin, E. Teitelbaum, J. H. Smet, D. Mahalu, V. Umansky, and A. Yacoby, *Nature (London)* **427**, 328 (2004).
- ³⁹A. Siddiki, S. Kraus, and R. R. Gerhardt, *Physica E (Amsterdam)* **34**, 136 (2006).
- ⁴⁰J. Huels, J. Weis, J. Smet, K. v. Klitzing, and Z. R. Wasilewski, *Phys. Rev. B* **69**, 085319 (2004).
- ⁴¹A. Siddiki and R. R. Gerhardt, *Phys. Rev. B* **68**, 125315 (2003).
- ⁴²J. G. S. Lok (private communication).
- ⁴³A. Manolescu and R. R. Gerhardt, *Phys. Rev. B* **51**, 1703 (1995).
- ⁴⁴A. Manolescu, *Phys. Rev. B* **52**, 2831 (1995).
- ⁴⁵S. Ihnatsenka and I. V. Zozoulenko, *Phys. Rev. B* **73**, 155314 (2006).
- ⁴⁶S. Ihnatsenka and I. V. Zozoulenko, *Phys. Rev. B* **74**, 201303(R) (2006).
- ⁴⁷S. Ihnatsenka and I. V. Zozoulenko, cond-mat/0607214 (to be published).
- ⁴⁸P. M. Morse and H. Feshbach, *Methods of Theoretical Physics*, Vol. II (McGraw-Hill, New York, 1953), p. 1240.
- ⁴⁹J. H. Davies, I. A. Larkin, and E. V. Sukhorukov, *J. Appl. Phys.* **77**, 4504 (1995).
- ⁵⁰T. Ando, A. B. Fowler, and F. Stern, *Rev. Mod. Phys.* **54**, 437 (1982).
- ⁵¹A. Siddiki and F. Marquardt, *Phys. Rev. B* **75**, 045325 (2007).
- ⁵²I. S. Gradshteyn and I. M. Ryzhik, *Table of Integrals, Series, and Products* (Academic Press, New York, 1994).
- ⁵³D. B. Chklovskii, K. A. Matveev, and B. I. Shklovskii, *Phys. Rev. B* **47**, 12605 (1993).
- ⁵⁴A. Siddiki and R. R. Gerhardt, in *Proceedings of the 15th International Conference on High Magnetic Fields in Semiconductor Physics*, edited by A. R. Long and J. H. Davies (Institute of Physics Publishing, Bristol, 2002).
- ⁵⁵U. Wulf and R. R. Gerhardt, in *Physics and Technology of Sub-micron Structures*, edited by H. Heinrich, G. Bauer, and F. Kuchar, Vol. 83 of Springer Series in Solid-State Sciences (Springer-Verlag, Berlin, 1988), p. 162.
- ⁵⁶T. Ando and Y. Uemura, *J. Phys. Soc. Jpn.* **36**, 959 (1974).
- ⁵⁷J. Groß and R. R. Gerhardt, *Physica B* **256-258**, 60 (1998).
- ⁵⁸J. P. Eisenstein, L. N. Pfeiffer, and K. W. West, *Appl. Phys. Lett.* **57**, 2324 (1990).
- ⁵⁹H. Rubel, A. Fischer, W. Dietsche, K. von Klitzing, and K. Eberl, *Mater. Sci. Eng., B* **B57**, 207 (1998).
- ⁶⁰M. Kellogg, J. P. Eisenstein, L. N. Pfeiffer, and K. W. West, *Phys. Rev. Lett.* **93**, 036801 (2004).
- ⁶¹K. Vakili, Y. P. Shkolnikov, E. Tutuc, E. P. De Poortere, and M. Shayegan, *Phys. Rev. Lett.* **92**, 226401 (2004).
- ⁶²R. D. Wiersma, J. G. S. Lok, S. Kraus, W. Dietsche, K. von Klitzing, D. Schuh, M. Bichler, H.-P. Tranitz, and W. Wegscheider, *Phys. Rev. Lett.* **93**, 266805 (2004).